

Chapter 6

Materials for Stereolithography

Serge Corbel, Olivier Dufaud, and Thibault Roques-Carmes

6.1 Introduction

Stereolithography (SL) is a rapid prototyping method for three-dimensional polymer part fabrication [3, 34, 49, 53, 63]. The technique is based on the process of photopolymerization, in which a liquid resin is converted into a solid polymer under laser irradiation [4, 34]. The models are produced by curing successive layers of the resin material until a three-dimensional object is formed. The advantages of stereolithography are its flexibility in manufacturing parts with different geometries and dimensions, its accuracy and its quickness. The challenge is to extend the stereolithography method to directly fabricate parts with complex shapes and good mechanical properties [30, 47, 58]. Recently, polymer/ceramic composite were successively fabricated by stereolithography [29, 46, 52, 62]. The manufacturing process requires the formulation of a photoreactive medium containing a photocurable resin and powders prior to laser exposure. Once polymerized, the photopolymer constitutes a tough matrix around ceramic particles.

For applications suspensions have to satisfy several requirements. It is mandatory to use stable dispersions during the fabrication process (over 1 h). This does call for the knowledge of blending particles and resin of different density. In the same time, the suspension viscosity should be less than 5 Pa s in order to ensure satisfactory layer recoating and reduce the time necessary to obtain a horizontal fresh layer [8]. Generally, the highly loaded ceramic/silica suspensions (nonhollow) are quite viscous [31]. Lately, the suspension must be UV curable with useful depth and resolution. The cured depth must be high enough to avoid an excessive time of fabrication. The adjunction of particles greatly modifies the behavior of the resin under photopolymerization due to the scattering and absorption of the incident light beam by the particles [56, 62]. We also have to manage that low shrinkage occurs during the liquid to solid polymerization process

S. Corbel (✉)

Laboratoire Réactions et Génie des Procédés, UPR 3349 CNRS,
Nancy-Université, 1, rue Grandville, 20451, 54001 Nancy Cedex, France
e-mail: serge.corbel@ensic.inpl-nancy.fr

6.2 Stereolithography Principle

In order to create 3D structures, the object is reproduced in a computer-aided-design (CAD) file [34]. Once the object to be built is designed, it is then numerically sliced in layers of a chosen thickness to define the different horizontal cross sections of the object to be manufactured. The 3D shape is broken down into a sequence of cross sections (layers), like the contours of a topographic map. The surface height is adjusted so that it is represented by one layer thickness. Then, the numerical data defining each of the sections are sequentially sent to the machine, in order to build them [34, 35]. Thus, a layer-by-layer coordinates of contour lines or surfaces are obtained. Using CAD information, laser beam radiation (355 nm Nd-YAG laser, Navigator I Vanadate with 20 kHz pulses frequency) is deflected vector by vector on the top of the surface of the liquid (Fig. 6.1).

The UV radiation is absorbed by the photoinitiator which in turn generated free radicals to initiate polymerization of a liquid monomer into a solid polymer. When a solid layer is performed, the deposition of a subsequent layer of photopolymerizable resin on the already polymerized part allowed continuing the manufacturing process. For this purpose, after the exposure step, the supporting platform containing the solid part is largely immersed in the reactive medium and then moved upward such that between the last cured layer and the resin surface there is a new layer of fresh resin. This was made thanks to a motor driving an elevator. The motorized vertical stage accuracy is of 5 μm for the motor controller used in the set-up. During this step of layer recoating, it is necessary to wait until the resin surface becomes completely flat and level in order to have accurate thickness control. This procedure is repeated until the polymer solid part is build. The stacking of the layers leads to a three-dimensional physical part. After a few hours, the platform is raised and the completed part removed. Resolution is clearly related to the film

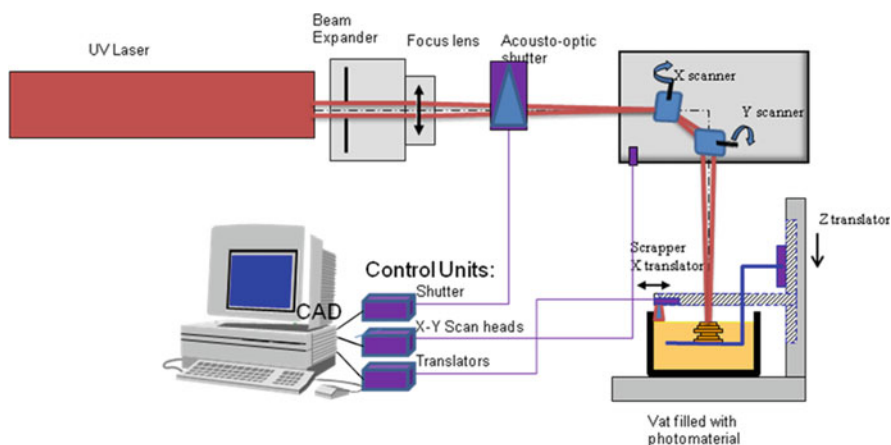
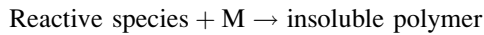
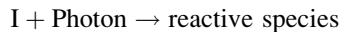


Fig. 6.1 Scheme of the stereolithography process (additive process layer by layer)

thickness and kinetics of photopolymerization and diffusion [53]. A typical layer thickness is 200 μm , line widths are similar. Thinner layers increase the part production time [6], but thicker layers may require longer laser exposure and also longer production times. The maximum part size is really limited by the size of the monomer bath and the dimensions of the photoreactor are convenient to the component's size typically $30 \times 30 \times 40$ cm. Other derived methods, such as liquid-crystal mask-based techniques [46, 52], DMD mask-based techniques [55] or two-photon absorption microfabrication processes have been developed recently [44]. In our case, experiments were carried out by conventional STL since it allows the use of commercial resins optimized for UV curing.

6.2.1 *Stereolithography of Polymers*

One of the main interests in the STL technique comes from the photopolymerization (curing) in long chain leading to a cross-linked network polymer. A photoinitiator, inside the reactive medium, produces free radicals or cations and induces the polymerization reaction. The irradiated liquid monomer polymerizes by a chain reaction into a solid polymer which does not dissolve in the remaining monomer. In the oversimplified mechanism:



I is a photochemical initiator directly leading, or not, to the reactive species which can be free radicals or ions, and M is a monomer or an oligomer. More complex mechanisms have been used [63], but it is not easy to take all the elementary steps into account and oxygen inhibition on photopolymerization [16]. The power of the lasers used to initiate such photopolymerization process is rather low, typically between 10 mW and 1 W, which makes STL technique economically attractive.

Most materials used are conventional epoxy, acrylate resins, or thermoplastics elastomers. The original monomers were combinations of multifunctional acrylates which formed cross-linked resins. This composition has several useful properties, such as low viscosity which assists smooth spreading of the liquid material, high photosensitivity, oxygen inhibition, low critical energy, controllable mechanical properties, and relative insensitivity to temperature and humidity changes [6]. The extent of their use in applications has been limited by their poor dimensional stability and by their high volume shrinkage. A major concern is the distortion induced by shrinkage during post-curing. Acrylates showed that the polymerization continued about 2 days after photoinitiation.

Newer photopolymerizable epoxies offer better properties. Thus, in contrast to acrylate resins, they have exceptionally low volume shrinkage and good dimensional stability.

STL has been broadly used as design, working, and master models in the industrial and medical sectors [33] and is currently applied in the medical field. Medical models built represent a new approach for surgical planning and simulation. This technique allows one to reproduce precisely anatomical objects as 3D physical models which can be looked and manipulated by the surgeon [50]. He has a realistic impression of complex structures and can simulate surgical procedures before a real surgical intervention. It is also very attractive in reconstructive surgery and implantation of prostheses, where each “part” has to be adapted to the unique anatomy of the patient and can be made in a short time. This raises the possibility of manufacturing simple prostheses during the course of an operation. For instance, in the reconstructive surgery field, cranioplasty implants have been successfully manufactured using the STL apparatus [21].

The use of STL is well suited for the fabrication of monolithic supports for photocatalysis applications [24]. Photocatalysis using TiO_2 as catalyst is an efficient advanced oxidation process in which the catalyst TiO_2 is deposited on a suitable support and activated by near UV light. It permits to create quickly several geometries which can be modified as necessary. Monolithic supports with complex 3D geometry, have been made in epoxy resin and then have been recoated with TiO_2 (Fig. 6.2b). They were successfully used in photocatalysis for cleaning air contaminated by volatile organic compounds and photocatalytic degradation of organic pollutants in water [22, 23].

STL allows the manufacture of various devices for microfluidic [11] and chemical engineering applications [14]. Microstructures, such as fluid mixers, fluid distributors, and heat exchanger [40], have been elaborated by conventional STL. For instance, Luo et al. examined experimentally the effects of constructal distributors on flow equidistribution in a multichannel heat exchanger [39]. The results showed that the integration of constructal distributors homogenized the fluid flow distribution and consequently led to a better thermal performance of the heat exchanger. Micro heat exchangers with internal channel dimensions in

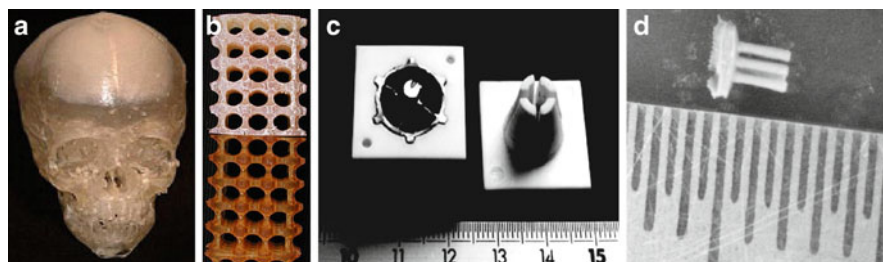


Fig. 6.2 Examples of parts pieces fabricated by stereolithography: (a) Skull in Polymer; (b) monolithic supports with TiO_2 coating; (c) Sintered ceramic mould loaded at 85 wt% alumina; (d) Piezoelectric ceramics: Rods loaded at 50 wt% PZT

the millimeter range have been manufactured [14]. The channel geometry was designed in order to produce local mixing of the fluid and to improve the fluid-side heat transfer. Even if the exchanger performance was low in terms of heat transfer due to their polymer walls, these three-dimensional parts allowed the characterization of mass transfer and pressure drop in such structure. Within this framework, research carried out to develop the STL of metallic structures would offer composites with higher thermal and electric conductivities. It also leads to channels and walls with higher mechanical resistance to fluid pressure.

6.2.2 Fabrication of Ceramic and Metal Components by Stereolithography

It is difficult to obtain a high level of hardness, high mechanical resistance to fluid pressure, thermal and electrical conductivity when photopolymer are used. In addition, photopolymers have limited applications because of the lack of biodegradability or sufficient mechanical strength. There are efforts to extend the system to other materials, such as ceramics and metals. The methods which are largely used for the fabrication of three-dimensional polymer parts [1, 10, 32, 43, 48, 54, 59–61], has been adapted to the process of three-dimensional ceramics and metallic pieces with final properties (mechanical, thermal, and electrical) closed to those obtained by classical processing techniques. The ultimate aim is the production of component in ceramic and metal material which can be obtained after the debinding and sintering step of the composite object.

The manufacturing process requires the formulation of a photoreactive medium containing a photocurable resin and powders (ceramic or metal particles) prior to laser exposure. Once polymerized, the photopolymer constitutes a tough matrix around ceramic particles and confers the cohesion of the green body. This organic phase is subsequently removed by an appropriate thermal treatment, then the sintering of the green part ensures the final properties of the ceramic piece. Various materials have already been successfully shaped in ceramic or metal-based composite materials by inserting different powders (silica, silicon nitride, alumina, hydroxyapatite, (zirconate titanate oxides PZT), aluminum, and copper) in acrylate or epoxy resins [7, 14, 19, 26, 30, 38, 45, 46, 52, 56]. Table 6.1 shows an overview of the various suspensions that have been used in such processes.

A candidate ceramic suspension for the process must satisfy several requirements:

- A high volume loading of particles is required to give dense and high quality ceramic pieces after debinding and sintering. In order to avoid deformation and cracking during binder removal, to reduce the shrinkage during sintering, and to obtain homogeneous and dense ceramic pieces after sintering, it is necessary to minimize the organic concentration in the suspension.
- The suspension viscosity should be less than 5 Pa s, in order to ensure satisfactory layer recoating and reduce the time necessary to obtain a horizontal fresh layer

Table 6.1 Suspension formulation and optical properties for direct fabrication by STL of composites. The values of D_p , E_c , C_d , and Q are calculated using (6.1) and (6.2)

UV curable resin	Powder nature	Particle size (μm)	Particle concentration % V/V	Δn ($n_{\text{part.}} - n_{\text{resin}}$)	D_p (μm)	E_c (mJ/cm ²)	C_d (μm) $E_0 = 2,600$ mJ/cm ²	Q
Epoxy	-	-	-	-	121	13.5	341	-
Acrylate	-	-	-	-	242	38.3	2,750	-
Epoxy	SiO ₂	5	50	-	137	12.7	323	0.0012
Acrylate	SiO ₂	3.5	50-60	0.03	140	6.15	800	0.033
Epoxy	Al ₂ O ₃	-	45	-	52	32.8	121	0.0037
Acrylate	Al ₂ O ₃	10	53	-	75	9.3	300	-
Acrylate	Al ₂ O ₃	4.4	50-60	0.23	68	4.8	350	0.086
Acrylate	Zircon	4.2	50-60	0.38	50	14.94	200	0.112
Acrylate	Silicon nitride	0.5	30	0.7	20	-	40	-
Acrylate	PZT	5	80 wt%	-	15	111	25	-
Acrylate	Al	6.5	80 wt%	-	12	1,200	17	-
Acrylate	Cu	3	60 wt%	-	10	-	-	-

completely flat [8, 9]. The increase of the viscosity of the resin leads to slow resin flows on the top of the build platform, which increases fabrication time and makes a convex mound on the surface of the building part after recoating cycle. If the viscosity is too high, the resin surface never becomes completely flat by gravity alone. Nevertheless, the viscosity of the suspension must be as low as possible to allow a good recoat of the liquid monomer on the polymerized underlayer [25].

- The movement of the scrapper is synchronized with the other operations (Fig. 6.1) and its speed is adapted to the rheology of the liquid. A suspension viscosity of 5 Pa s, is set at the maximum resin viscosity in conventional stereolithography with scrapper to ensure a satisfactory layer recoating. Higher viscosity leads to a paste rather than a liquid which is not possible to process with a conventional STL machine and need special scrapper to spread such pastes.
- The suspension must be UV curable with useful depth and resolution. The cure depth must be high enough to avoid an excessive time of fabrication. The adjunction of particles greatly modifies the behavior of the resin under photopolymerization due to the scattering and absorption of the incident light beam by the particles. The reactivity of an STL resin is characterized by two parameters (D_p and E_c) that define the photosensitivity of UV curable resin during the process. The theoretical expression of the cured depth (C_d , i.e., the thickness of the gelled resin) is derived from the Beer–Lambert law of absorption and can be written as [53]:

$$C_d = D_p \ln\left(\frac{E}{E_c}\right) \quad (6.1)$$

where D_p is the penetration depth of the resin, E and E_c are the laser exposure on the resin surface and critical exposure of the resin at the laser wavelength, respectively. Critical exposure E_c is the laser energy below which the polymerization does not occur. A good resin for STL is characterized by low values of E_c , in order to start the reaction with low energy dose, and by high values of D_p , in order to optimize the cured thickness.

In presence of scattering particles, the penetration depth D_p is expressed as [25]:

$$D_p = \frac{2}{3} \left(\frac{d}{\phi Q} \right) \left(\frac{n_0}{\Delta n} \right)^2 \quad (6.2)$$

where d is the mean particle size of the powders, ϕ is the volume fraction of ceramics in the suspension, n_0 is the refractive index of the monomer solution, Δn is the refractive index difference between the ceramic and the monomer solution, and Q is the scattering efficiency term. D_p is a function of the volume concentration of powder, the particle diameter and the refractive index difference between the UV curable solution and powder.

The adjunction of particles greatly modifies the behavior of the resin under photopolymerization due to the scattering and absorption of the incident light beam by the particles [56, 62]. It was found that due to light scattering, the fabricated line is

wider in width and smaller in depth (low D_p) compared with polymeric fabrication at the same condition (Table 6.1). It was also demonstrated that the higher the refractive indexes difference between the particle and the resin, the stronger the light scattering. The scattering effect can be greatly minimized by choosing the ceramic particles that have the refractive index close to that of the solution. Silica is special in having a refractive index close to that of the resin. Using silica powders characterized by lower values of Δn leads to sufficient depth C_d and D_p values ($C_d = 300 \mu\text{m}$ and $D_p = 140 \mu\text{m}$). The alumina suspension shows higher values of Q as compared to silica suspension (Table 6.1). Light scattering by alumina and zircon is much stronger and cure depths are lower ($C_d = 200 \mu\text{m}$ and $D_p = 70 \mu\text{m}$). Satisfactory cure depths could be achieved but at the cost of exposure energies about 100 times that of unfilled resins, with a consequent proportional expected increase in build time. Light scattering could be decreased by the use of dyes to tune the refractive index of the resin closer to that of the ceramic [62]. For a higher refractive index difference (silicon nitride), the cure depth is more attenuated ($C_d = 40 \mu\text{m}$ and $D_p = 20 \mu\text{m}$) and becomes insufficient for STL applications. The penetration thickness of the laser is the lowest in the case of PZT ($C_d = 25 \mu\text{m}$ and $D_p = 15 \mu\text{m}$), aluminum ($C_d = 17 \mu\text{m}$ and $D_p = 12 \mu\text{m}$), and copper, due to the predominance of light absorption and scattering [14]. This implies a very delicate processing of piezoelectric ceramic and metal by STL apparatus because of the spreading of thin layers (20 to 10 μm). The STL process which was used for polymer or alumina suspensions shaping is not convenient for the deposition of layers thinner than 50 μm . A new system was developed in the laboratory consisting of injecting nitrogen through a nozzle. The nitrogen flow can spread a layer of a thickness between 6 and 40 μm [14, 45]. The pressure applied by the nitrogen stream on the suspension acted as a substitute for the mechanical pressure of the former scraper.

Stereolithography has been used to fabricate metal and ceramic parts. After debinding and sintering steps, the resulting ceramic parts have been used either as functional components or as molds for investment casting. The major drawback of the classical fabrication of complex ceramic parts is the cost of the mold, the difficulties to obtain different complicated cross sections and the processing time required to develop the first prototype. STL offers a unique opportunity to fabricate, without using costly molds, complex ceramic parts [5, 7, 14, 15, 19, 29, 30, 36, 46, 62] (Alumina and silica) with final properties (mechanical properties) similar to those obtained by classical processing techniques in a much reduced time and cost (Fig. 6.1) (Piezoelectric ceramics like lead zirconate titanate oxides ($\text{Pb}(\text{Zr},\text{Ti})\text{O}_3$) PZT dedicated to microelectromechanical systems (MEMS), microfluidic applications, and medical imaging applications have been fabricated by STL. The characterization of PZT films, 80–130 μm thick, on silicon substrate showed piezoelectric properties (dielectric permittivity, tangent loss, and remanent polarization) comparable with those of PZT thick films fabricated by other methods [36]. These structures were also integrated in MEMS for advanced piezoelectric microsensors and microactuators with high energy density. Dufaud et al. [15], have designed and fabricated transducers with 45%vol of PZT similar in shape to those typically obtained with injection molding methods. Microtransducers and micropumps have been elaborated and

their contribution in sensing, control, and hydrodynamic fields has been shown [14]. The technique allows the manufacture of various devices for microfluidic applications. A polymer micropump, with a PZT transducer integrated within the upper membrane, was successfully fabricated. PZT/polymer composites have shown excellent aptitudes in the domain of ultrasound medical imaging since the epoxy matrix lowered the acoustic impedance of the composite and made it close to human body impedance [51]. Promising results were also obtained with biocompatible ceramics, such as hydroxyapatite suspensions for medical implant design [12, 27].

Mauzon et al. [45] have demonstrated the possibility of metal components fabrication by direct STL. Aluminum and copper cylinders of 5 mm diameters, microgear, and cube have been realized [38].

6.3 Aluminum Components Fabrication

6.3.1 Raw Materials

Aluminum powders were provided by Goodfellow with an average size d_{50} of 6.5 μm . The 90th percentile particle size (d_{90}) was approximately 12 μm . During this study, aluminum particles are considered as spherical, which was confirmed by optical microscopy. The density of aluminum is 2.7 g/cm^3 and their refractive index is 1.44.

Different resins were used as binders: on the one hand, epoxy or epoxy-acrylates (3,4-epoxycyclohexylmethyl-3,4-epoxycyclohexyl carboxylate trimethylolpropane triacrylate called Somos 6100, Dupont and RPCure 200 AR, RPC) and on the other hand, acrylates (2,2'-bis[4-(methacryloxyethoxy)phenyl]propane called Diacryl 101, Akzo Nobel Chemicals, and 1,6-hexanediol diacrylate called HDDA, UCB) [13].

To improve monomers reactivity, DMPA (2,2'-dimethoxy-2-phenylacetophenone, Aldrich) was used as UV photoinitiator. The addition of a dispersing agent, coating particles surface, was compulsory to ensure dispersions homogeneity and stability. A phosphoric ester (Beycostat c213, CECA) was then chosen as regard as previous experiments [17].

6.3.2 Preparation of Photocurable Suspensions

At first, aluminum powder was diluted in a solvent acetone/ethanol. Then, the metal was coated with 1.5 wt% dispersant with respect to the metal amount (Sonic Dismembrator 550, Fisher Scientific). The solvent was evaporated at room temperature to allow ester adsorption onto particles surfaces. After drying, powder was deagglomerated with a 50 μm sieve. Granulometric analyses have shown the absence of aggregates larger than 30 μm .

Finally, aluminum was mixed with resin and 1 wt% UV photoinitiator with respect to the metal, during 40 min by ball milling (300 rpm – Retsch PM400, Fisher Scientific).

6.3.3 Characterization

Rheological measurements were carried out thanks to a stress-controlled viscosimeter (CSL-100, Carri-Med) in a cone-plane setting on shear rate range $\dot{\gamma}$ of 0.1–300 s⁻¹ at various temperatures from 283 to 373 K (10–100°C). Moreover, the stability of aluminum suspensions was checked by sedimentation rate experiments.

The thickness (E_p) and the width (L_p) of a polymerized element has been determined by optical profilometry.

Finally, the features of 3D parts were investigated thanks to a helium pycnometer (Accupyc 1330) for density measurements and to a digital multimeter for conductivity measurements.

6.4 Aluminum Suspensions Properties

6.4.1 Rheological Behavior

The influences of binder nature, fillers loading, and temperature on the suspensions rheological behavior was investigated in order to improve the layers recoating by scrappers or gas injection nozzles.

First of all, several resins, standard in stereolithography process, were tested with the stress-controlled viscosimeter. Among these monomers, only HDDA (1,6-hexanediol diacrylate) has revealed a plastic viscosity clearly lower than 1 Pa s at different shear rates and especially for $\dot{\gamma}$ greater than 40 s⁻¹, which is the case with the recoating systems available. Higher viscosities, in particular with high filler loading, will increase the probability of heterogeneous surfaces occurrence or problems in layers recoating due to a viscoelastic behavior. As a consequence, HDDA was chosen as organic binder for aluminum suspensions. It is worth to note that HDDA shows an important shear-thinning behavior, which is useful for dispersions spreading [17].

The rheological behavior of aluminum suspensions was studied for different fillers loading. However, when loading is lower than approximately 70 wt%, parts could not be properly sintered and on the other hand, loading greater than 90 wt% imply dispersions with too high viscosities.

Experiments were thus mainly carried out with 80 wt% aluminum in HDDA monomer. The shear-thinning behavior of the suspensions, (Fig. 6.3), has been fitted by a Sisko model:

$$\tau = \eta_{\infty} \dot{\gamma} + k \dot{\gamma}^n$$

where k is the consistency coefficient in Pa s and η_{∞} is the high-shear Newtonian limit.

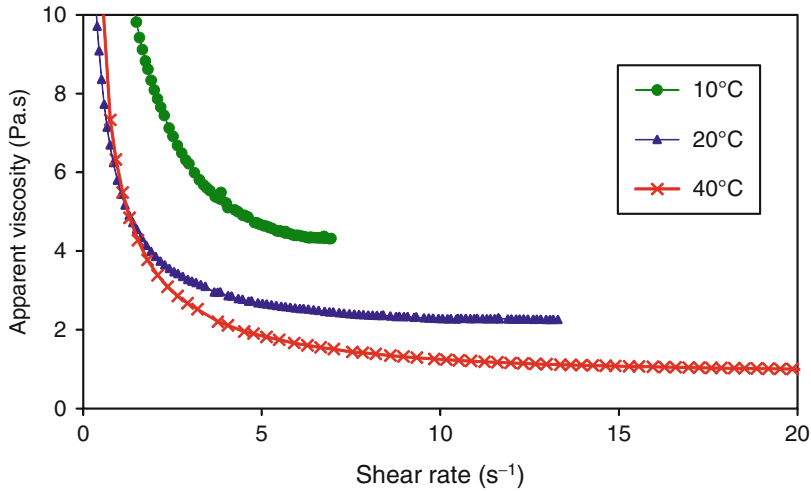


Fig. 6.3 80 wt% aluminum suspensions viscosity versus shear rates at various temperatures [45]

In order to compensate the viscosity increase due to fillers addition, the heating of the suspensions was studied. As shown on Fig. 6.3, when the temperature increases from 293 to 353 K, the apparent viscosity η drops from 2.58 to 0.33 Pa s. This evolution is well represented by an Arrhenius relation:

$$\eta = A \exp\left(\frac{E_a}{RT}\right)$$

where E_a , the activation energy is $34,430 \text{ J mol}^{-1}$, which is close to these of HDDA monomer ($32,000 \text{ J mol}^{-1}$), and A , the pre-exponential factor is $2.35 \cdot 10^{-6} \text{ Pa s}$. Previous experiments carried out on PZT suspensions in HDDA have shown that E_a was also in this range. As a consequence, this parameter probably only depends on binder nature Fig. 6.4.

For further tests, the suspension temperature was limited to 313 K in order to avoid unwanted resin reaction in the presence of photoinitiator.

6.4.2 Dispersions Reactivity

The dispersion reactivity was verified by cured depth (E_p) and width (L_p) measurements. These parameters depend on the density of energy (DE in J/m^2) received by the suspension during a unit of time:

$$\text{DE} = \frac{2P_0}{W_0 v \pi}$$

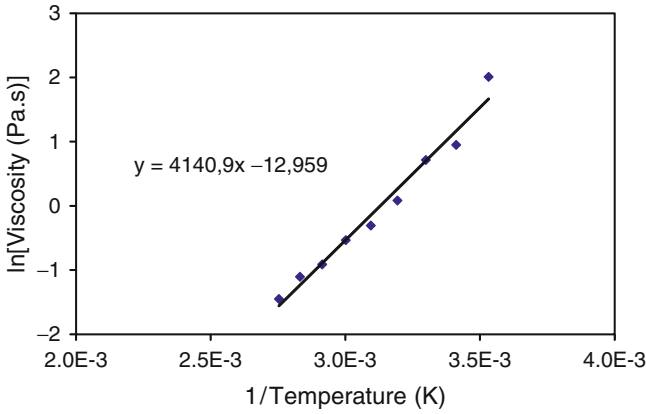


Fig. 6.4 Representation of the Arrhenius relation between suspensions viscosity and temperature [45]

The effects of DE variations on cure width and depth were observed by changing v , the scanning velocity of the laser beam. Laser beam radius w_0 and irradiation power P_0 were kept constant with the respective values:

$$w_0 = 150 \mu\text{m} \text{ and } P_0 = 60 \text{ mW}.$$

According to Beer–Lambert’s law, the polymerization depth is defined by:

$$E_p = D_p \ln\left(\frac{DE}{DE_c}\right)$$

where DE_c is the minimum density of energy necessary to begin the polymerization and D_p , the laser depth of penetration. Similarly, the polymerization width is represented as follows:

$$L_p = \frac{w_0}{\sqrt{2}} \sqrt{\ln\left(\frac{DE}{DE_c}\right)}$$

Increases of polymerized width and depth shown on Fig. 6.5 are consistent with previous observations. Even if there are three polymerization regions for aluminum suspensions, only two of them could be observed on Fig. 6.5 [28]. At very low energy of irradiation, the inhibition of polymerization by oxygen is predominant and prevents the polymerization [18]. When the polymerization starts and below about 3 J/cm², the polymerization rate is not affected by oxygen, the polymerization reaction is fast with a high slope of the curve. At higher energy, the free radicals are likely to react with each other than to form polymer. Then, an increase of the irradiation does not lead to high significant modifications of the depth or width curing and the slope is lower.

Finally, for highly loaded aluminum suspensions, the vertical depth of curing varies from 5 to 20 μm , whereas the lateral width ranges between 250 and 500 μm . Thus, both thick films and 3D components could be fabricated from these dispersions.

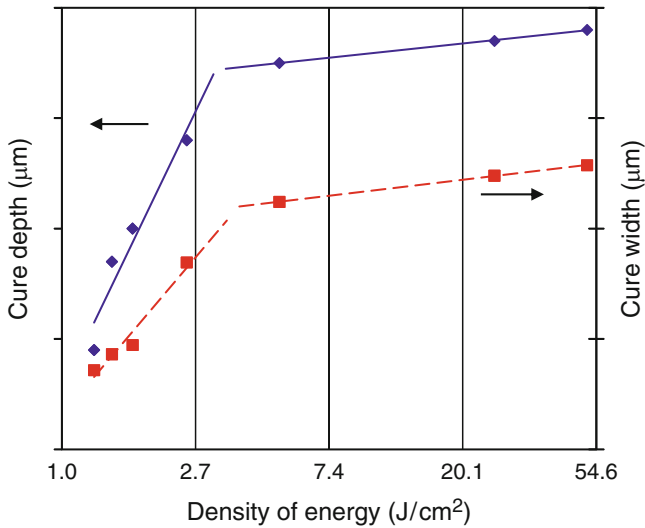


Fig. 6.5 Cure depth and width (*dashed*) versus $\ln(\text{DE})$ for a 80 wt% aluminum suspensions [45]

6.5 Three Dimensional Parts Fabrications

6.5.1 Green Parts Fabrications

The aluminum suspension used for green parts fabrication was loaded at 80 wt% in HDDA monomer and kept at 40°C. A new recoating system, based on an oxygen injection nozzle, was developed to allow the deposition of suspensions layers with depth ranging between 6 and 40 µm. In these conditions, the oxygen inhibition on polymerization kinetics and consequently the gain on process accuracy were used to reach optimum lateral and vertical resolutions [13]. Green parts were carefully rinsed with isopropanol.

Two kinds of objects were fabricated by direct stereolithography of aluminum suspensions: on the one hand, metal sheets loaded at 80 wt% aluminum, on the other hand, multilayers components (Fig. 6.6).

Aluminum thick films with an average depth ranging from 4 to 20 µm were laid on glass plates, ceramic plates as well as on copper films. Due to aluminum electrical properties and to layers thickness, these sheets could probably be used as electrodes in MEMS applications.

Three-dimensional structures were also fabricated (Fig. 6.7). The microgear shown on Fig. 6.7 is constituted with 280 layers of 15 µm thickness. Aluminum/polymer composites with cube shape were fabricated in order to be sintered and to be used as demonstrators for conductivity measurements.

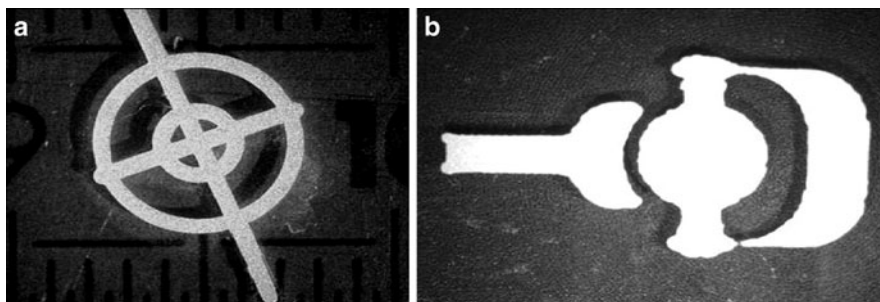
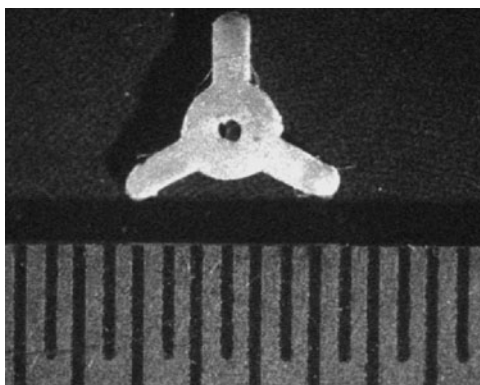


Fig. 6.6 Examples of aluminum sheets loaded at 80 wt% aluminum; (a) one-layer target – 15 μm thick; (b) first layer of a mechanical articulation [45]

Fig. 6.7 Examples of aluminum components: microgear loaded at 80 wt% aluminum [45]



6.5.2 Sintering

The green parts were debinded and sintered in order to improve their mechanical resistance and to study their electrical, and soon, their thermal properties. Thermogravimetric analysis was carried out to determine the optimum temperature for polymer debinding.

The density of the sintered parts was calculated from analyses performed with a pycnometer (AccuPyc 1330).

As shown on Fig. 6.8, the density of the sintered parts increases with the sintering temperature. At 773 K, the green part is debinded and its density is equal to aluminum one. However, the poor mechanical properties of the parts prevent them to be handling without crumbling. Over 873 K, surfaces are covered with alumina oxide. Indeed, the oxidation of aluminum into alumina begins at 623 K and is complete at 1,313 K. Finally, over 933 K, which is aluminum melting temperature, parts density tends to become the alumina density, with a lack of their electrical properties.

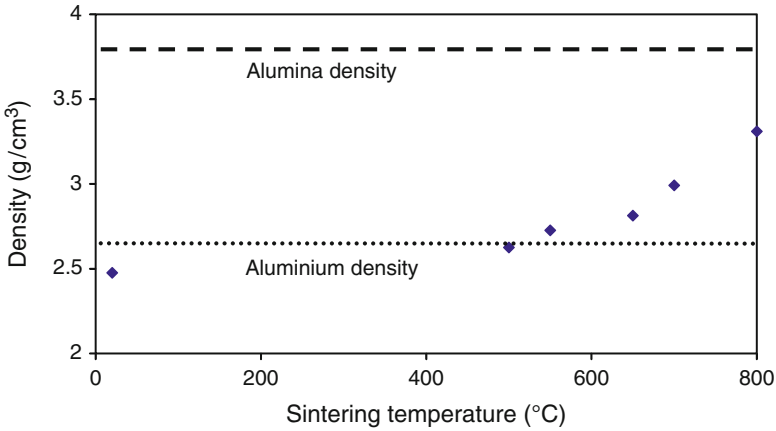


Fig. 6.8 Evolution of the sintered components density versus the sintering temperature [45]

Thus, a temperature of 873 K was chosen in order to avoid the alumina formation. Moreover, the rate of sintering seems to be optimal at about 793 K.

6.5.3 Metal Components Properties

To determine the conductivity of aluminum parts after sintering, their electric resistance was measured between two points distant of 5 mm. Two models were used to exploit these measurements [20]:

1. On the one hand, an empirical relation based on electrical conductivity of electrodeposited nickel foams:

$$\lambda = \frac{1}{4}(1 - \Phi)\lambda_s \quad (6.3)$$

2. On the other hand, based on a theoretical [20] model related to octahedral arrays of metallic wires:

$$\lambda = \frac{(1 - \Phi)}{3 \left[1 - 0.121(1 - \Phi)^{1/2} \right]} \lambda_s \quad (6.4)$$

where λ is the electric conductivity, λ_s is the conductivity of the solid and Φ is the average porosity.

The parts porosity was modified by changing the fillers content of metallic suspensions before manufacturing. After stereolithography and sintering steps, measurements show that the volume withdrawal was approximately 10%.

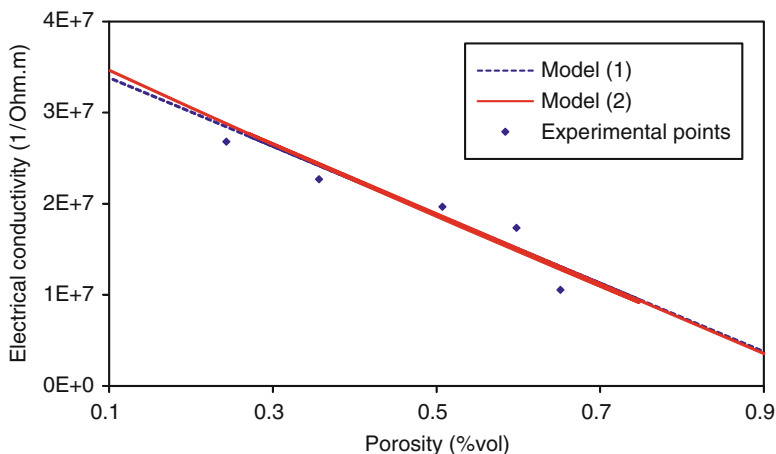


Fig. 6.9 Evolution of aluminum parts electrical conductivity versus porosity [45]

It should be noticed on Fig. 6.9 that both models satisfactorily fit the experimental points. No measurements have been carried out for porosity greater than 65% volume because of the poor mechanical properties of the parts. Moreover, it is highly likeable that no electrical properties would be found below the percolation threshold of aluminum particles.

As a conclusion, electrical conductivities of aluminum parts have been determined and are in accordance with literature models. On top of the advantages due to parts electrical properties, it is also possible to determine their porosity by means of electric resistance measurements.

6.6 Conclusions

Small components or sheets in different material can be made by using direct stereolithography process. From the adequate photocurable suspension of metal or ceramic whose rheological behavior and the dispersion reactivity have been perfectly identified, three-dimensional parts have been built by using a UV laser irradiation with a suitable beam diameter. The technique has been followed by a step of sintering in order to improve the mechanical resistance of the green parts. The determination of the sintering temperature is a crucial point: a too high temperature could alter the quality of the metal and a too low one could be inefficient treatment. Finally, some sintered parts in aluminum were successfully obtained.

This result and the design flexibility, fabrication quickness, and the accuracy of direct stereolithography lead us to think that direct stereolithography is a suitable

process to realize small functional parts in alternative with microstereolithography process.

Indeed, the application's field of such fabrications is vast and could be widely used. However, some adjustments remain before exploiting industrially this process.

Acknowledgments The authors would like to acknowledge Jean François Rémy (LSGC) for the granulometric measurements.

References

1. Abe, F., Osakada, K., Shiomi, M., Uematsu, K., Matsumoto M, The manufacturing of hard tools from metallic powders by selective laser melting, *Journal of Materials Processing Technology*, 111(1–3), (2001), 210–213.
2. Allanic A-L., P. Schaeffer, French Patent n FR2790 418-A1, (1999).
3. André J.C., A. Le Méhauté, O. De Witte, French Patent, 8, (1984), 411, 241.
4. André J.C., S. Corbel, *Stéréolithographie Laser*, Polytechnica, Paris, 1994, 26.
5. Bertsch A., S. Jiguet, P. Renaud, *Journal of Micromechanics and Microengineering* 14, (2004), 197–203.
6. Calvert P., R. Crockett, *Chemistry of Materials*, 9, (1997), 650–663.
7. Chartier T., C. Chaput, F. Doreau, M. Loiseau, *Journal of Materials Science* 37 (2002), 3141–3147.
8. Chartier T., C. Hinczewski, S. Corbel, *Journal of the European Ceramic Society* 19 (1999), 67–74.
9. Chartier T., M. Ferrato, J.F. Baumard, G. Coudamy, *Acta Ceramica* 6 (6), (1994), 17.
10. Choi, D. S., Lee, S. H., Shin, B. S., Wang, K. H., Song, Y. A., Park, S. H., Jee, H. S, Development of a direct metal freeform fabrication technique using CO₂ laser welding and milling technology, *Journal of Materials Processing Technology*, 113, (2001), 273–279.
11. Cia L., S. Mantell, D. Polla, *Sensors Actuators A* 94, (2001), 117–125.
12. Dhariwala B., E. Hunt, T. Boland, *Tissue Engineering*, 10, (2004), 1316.
13. Dufaud O., Corbel S, Oxygen diffusion in ceramics suspensions for stereolithography, *The Chemical Engineering Journal*, 4082, (2002), 1–8.
14. Dufaud O., H. Le Gall, S. Corbel, *Trans. IChemE, Part A, Chemical Engineering and Design* 83, (2005), 133–138.
15. Dufaud O., P. Marchal, S. Corbel, *Journal of the European Ceramic Society* 22 (2002), 2081–2092.
16. Dufaud O., S. Corbel, *Chemical Engineering Journal*, 92 (1–3), (2003), 55–62.
17. Dufaud, O. (2002), *Prototypage rapide de composites céramiques fonctionnels*, Ph.D. Thesis, Institut National Polytechnique de Lorraine, 2002.
18. Dufaud, O., Corbel S, Stereolithography of PZT ceramic suspensions, *Rapid Prototyping Journal*, 8(2), (2002), 83–90.
19. Esposito C. Corcione, A. Greco, F. Montagna, A. Licciulli, A. Maffezzoli, *Journal of Materials Science* 40 (2005), 4899–4904.
20. Feng, Y., Zheng, H., Zhu, Z., Zu, F, The microstructure and electrical conductivity of aluminum alloy foams, *Materials Chemistry and Physics*, 78, (2002), 96–201.
21. Forouta M., B. Fallahi, S. Mottavahi, S. Mottavalli, M. Dujovny, *Critical Reviews in Neurosurgery*, 8, (1998), 203–208.
22. Furman M., S. Corbel, H. le Gall, O. Zahraa, M. Bouchy, *Chemical Engineering Science* 62, (2007), 5312–5316.
23. Furman M., S. Corbel, H. le Gall, O. Zahraa, M. Bouchy, *Virtual Modeling and Rapid Manufacturing*, (2005), 589–593.

24. Gerven T.V., G. Mul, J. Moulijn, A. Stankiewicz, *Chemical Engineering and Processing* 46, (2007), 781–789.
25. Griffith M.L., J.W. Halloran, *Journal of the American Ceramic Society*, 79 (10) (1996), 2601–2608.
26. Griffith M.L., J.W. Halloran, *Manufacturing Science and Engineering*, 2, (1994), 529–534.
27. Griffith M.L., T-M Chu, W. Wagner, J.W. Halloran, *Solid Freeform Fabrication Conf. (SFF'95)*, (1995), 31–38.
28. Griffith, M. L. (1995), *Stereolithography of ceramics*, Ph.D. Thesis, University of Michigan, 1995.
29. Hinczewski C., S. Corbel, T. Chartier, *Journal of the European Ceramic Society* 18 (1998), 583–590.
30. Hinczewski C., S. Corbel, T. Chartier, *Rapid Prototyping Journal*, 4(3), (1998), 104.
31. Hinczewski, C., Corbel, S., Chartier, T, *Stereolithography for the fabrication of ceramic three-dimensional parts*, *Rapid Prototyping Journal*, 4(3), (1998), 104–111.
32. Ikuta, K., Hirowatari, K, *Real three dimensional micro fabrication using stereolithography and metal molding*, MEM'93, *Proceedings An Investigation of Micro Structures, Sensors, Actuators, Machines and Systems*. IEE. (<http://dx.doi.org/10.1109/MEMSYS.1993.296949>), *Proceedings of IEEE Symposium*, (1993), 42–47.
33. Im Y.G., S.I. Chung, J.H. Son, Y.D. Jung, J.G. Jo, H.D. Jeong, *Journal of Materials Processing Technology* 130–131, (2002), 372–377.
34. Jacobs P.F., *Rapid Prototyping and Manufacturing: Fundamentals of Stereolithography* (Society of Manufacturing Engineers Publishers, Dearborn, 1992).
35. Jacobs, P. F. (1996), *Stereolithography and other RP&M technologies*, Soc. of Manuf. Engineers, Dearborn (1996)
36. Jiang X.N., C. Sun, X. Zhang, B. Xu, Y.H. Ye, *Sensors and Actuators A*: 87, (2000), 72–77.
37. Kindernay J., A. Blazkova, J. Ruda, V. Jancovicova, Z. Jakubicova, *Journal of Photochemistry and Photobiology A: Chemistry* 151, (2002), 229–236.
38. Lee J.W., I.H. Lee, D.W. Cho, *Microelectronic Engineering* 83, Issues 4–9, (2006), 1830–1866.
39. Luo L., D. Tondeur, H. le Gall, S. Corbel, *Applied Thermal Engineering* 27, (2007), 1708–1714.
40. Luo L., D. Tondeur, *International Journal of Thermal Science* 44, (2005), 1131–1141.
41. Luo L., Y. Fan, W. Zhang, X. Yuan, N. Midoux, *Chemical Engineering Science* 62, (2007), 3605–3619.
42. Luo L., Z. Fan, H. le Gall, X. Zhou, W. Yuan, *Chemical Engineering and Processing* 47, (2008), 229–236.
43. Male, A. T., Chen, Y. W., Pan, C., Zhang, Y. M, *Rapid prototyping of sheet metal components by plasma-jet forming*, *Journal of Materials Processing Technology*, 135, (2003), 340–346.
44. Maruo S., S. Kawata, *Journal of Microelectromechanical Systems*, 7 (4), (1998), 411–415.
45. Mauzon A., O. Dufaud, H. Le Gall, S. Corbel, *10èmes Assises Européennes de Prototypage Rapide*, 2004.
46. Monneret S., C. Provin, H. Le Gall, S. Corbel, *Microsystem Technologies* 8, (2002), 368–374.
47. Müller, H., Sladojevic, J, *Rapid tooling approaches for small lot production of sheet-metal parts*, *Journal of Materials Processing Technology*, 115, (2001), 97–103.
48. Nakagawa, T., Makinouchi, A., Wei, J., Shinizu, T, *Application of laser stereolithography in FE sheet-metal forming simulation*, *Journal of Materials Processing Technology*, 50, (1995), 318–323.
49. Nee A.Y.C., J.Y.H. Fuh, T. Miyazawa, *Journal of Materials Processing Technology* 113, (2001), 262–268.
50. Petzold R., H.F. Zeilhofer, W.A. Kalender, *Computerized Medical Imaging and Graphics* 23, (1999), 277–284.
51. Pilgrim S.M., A.E. Bailey, M. Massouda, F.C. Poppe, A.P. Ritter, *Ferroelectrics* 160, (1994) 383–390.
52. Provin C., S. Monneret, *IEEE Transactions on Electronics Packaging Manufacturing* 25, (2002) 59–63.

53. Schaeffer P., A. Bertsch, S. Corbel, J.Y. Jézéquel, J.C. Andre, *Journal of Photochemistry and Photobiology A: Chemistry* 107, (1997) 283–290.
54. Shinizu, T., Murakoshi, Y., Wang, Z., Maeda, R., Sano, T, Microfabrication techniques for thick structure of metals and PZT, Symposium on Design, Test and Microfabrication of MEMS and MOEMS, Paris, France, SPIE vol. 3680, (1999), 72–477.
55. Sun C., N. Fang, D.M. Wu, X. Zhang, *Sensors and Actuators A* (2005).
56. Sun C., X. Zhang, *Journal of Applied Physics* 92 (8), (2002) 4796–4802.
57. Tondeur D., L. Luo, *Chemical Engineering Science* 59, (2004) 1799–1813.
58. Voelkner, W, Present and future developments of metal forming: selected examples, *Journal of Materials Processing Technology*, 106, (2000), 236–242.
59. Wang, J., Wei, X P., Christodoulou, P., Hermanto, H. (2004), Rapid tooling for zinc spin casting using arc metal spray technology, *Journal of Materials Processing Technology*, 146, (2004), 283–288.
60. Wu, G., Langrana, N. A., Sadanji, R., Danforth, S. (2002), Solid freeform fabrication of metal components using fused deposition of metals, *Materials and Design*, 23, (2002), 97–105.
61. Yarlagadda, P., Ilyas, I. P., Christodoulou P. (1993), Development of rapid tooling for sheet metal drawing using nickel electroforming and stereolithography processes, *Journal of Materials Processing Technology*, 111, (2001), 286–294.
62. Zhang X., X.N. Jiang, C. Sun, *Sensors and Actuators A*: 77, (1999) 149–156.
63. Zissi S., A. Bertsch, J.Y. Jézéquel, S. Corbel, D.J. Lougnot, J.C. Andre, *Microsystem Technologies* 2, (1996) 97–102.